The Polarimetric L-Band Imaging Synthetic Aperture Radar (PLIS): Description, Calibration, and Cross-Validation

Liujun Zhu, Jeffrey P. Walker, Nan Ye, Christoph Rüdiger, *Senior Member, IEEE*, Jorg M. Hacker, Rocco Panciera, Mihai A. Tanase, Xiaoling Wu, Douglas A. Gray, Nick Stacy, Alvin Goh, Heath Yardley, and Jim Mead

***Abstract*—The polarimetric L-band imaging synthetic aperture radar (PLIS) is a high spatial resolution (better than 6 m) airborne synthetic aperture radar system that has been dedicated to scientific research into civilian applications since 2010. The weight of PLIS is ∼38 kg, allowing it to be installed aboard small low-cost aircraft, with two antennas used to measure the full backscatter matrix for a swath between 15° and 50° on each side of the flight direction. Calibration based on a total of 96 calibration points and a homogeneous forest during the two recent soil moisture active passive experiments (SMAPEx-4 and 5) showed an overall radiometric accuracy of 0.58 dB (root-mean-square error) over trihedral passive radar calibrators. Independent evaluation based on polarimetric active radar calibrators showed an amplitude imbalance of 0.17 dB with a standard deviation of 0.15 dB and a phase imbalance of 3.87° with a standard deviation of 2.86°. Two calibrated phased-array L-Band synthetic aperture radar-2 (PALSAR-2) images with different observation modes (ScanSAR and Stripmap) were compared with the calibrated PLIS images. The agreement between PALSAR-2 Stripmap and PLIS had a root mean square difference of 1.27 dB and a correlation coefficient of 0.87. Further comparisons over different landcover types confirmed that homogeneous forest and grassland areas constitute optimal targets for cross-validation and/or calibration.**

***Index Terms*—Calibration and validation, cross-calibration, phased-array L-Band synthetic aperture radar-2 (PALSAR-2), polarimetric L-band imaging SAR (PLIS), synthetic aperture radar (SAR).**

Manuscript received April 8, 2018; revised September 17, 2018; accepted September 17, 2018. Date of publication October 17, 2018; date of current version November 27, 2018. The PLIS was developed using funds from the Australian Research Council's Linkage Infrastructure, Equipment and Facilities funding scheme (LE0882509) while the SMAPEx-4 and 5 field campaigns were supported by an Australian Research Council Discovery Project (DP140100572). *(Corresponding author: Liujun Zhu.)*

L. Zhu, J. P. Walker, N. Ye, C. Rüdiger, and X. Wu are with the Department of Civil Engineering, Monash University, Clayton, VIC 3800, Australia (e-mail: liujun.zhu@monash.edu; jeff.walker@monash.edu; ye.nan@monash.edu; chris.rudiger@monash.edu; xiaoling.wu@monash.edu).

J. M. Hacker is with the Airborne Research Australia School of the Environment, Flinders University, Adelaide, SA 5106, Australia (e-mail: jorg.hacker@flinders.edu.au).

R. Panciera is with the United Nations Children's Fund, New York, NY 10017 USA (e-mail: pancerarocco@gmail.com).

M. A. Tanase is with the Department of Geology, Geography, and Environment, University of Alcalá, Madrid 28801, Spain (e-mail: mihai@tma.ro).

D. A. Gray is with the School of Electrical and Electronic Engineering, The University of Adelaide, Adelaide, SA 5005, Australia (e-mail: douglas.gray@adelaide.edu.au).

N. Stacy, A. Goh, and H. Yardley are with the Defence Science and Technology Group, Edinburgh, SA 1500, Australia (e-mail: nick.stacy@dsto.defence.gov.au; alvin.goh@dsto.defence.gov.au; heath.yardley@dsto.defence.gov.au).

J. Mead is with the ProSensing, Amherst, MA 01002 USA (e-mail: mead@pros-ensing.com).

Color versions of one or more of the figures in this paper are available online at http://ieeexplore.ieee.org.

Digital Object Identifier 10.1109/JSTARS.2018.2873218

I. Introduction

SINCE the conception of synthetic aperture radar (SAR) in the 1950's [1], the list of applications that use SAR as a remote sensing tool has rapidly expanded, including fields as diverse as defense, geology, agriculture, forestry, disaster management, oceanography, cryospheric monitoring, and even archaeology. These applications have recently entered a new era, with operational use now possible due to the number of existing and planned SAR missions in the next decade [2].

Despite the increased availability of spaceborne SAR data, airborne SAR systems still play a vital role in the development, implementation, testing and verification of potential spaceborne SAR applications. Currently, there are several airborne SAR systems developed by different organizations throughout the world [2]. Some of the most commonly used include the AIRborne synthetic aperture radar (AIRSAR), uninhabited aerial vehicle SAR (UAVSAR) [3] and the digital beamforming synthetic aperture radar [4] of the National Aeronautics and Space Administration (NASA); E-SAR and F-SAR of the German Aerospace Center (DLR); and the Polarimetric and Interferometric AIRSAR L2 (Pi-SAR-L2) of the Japan Aerospace Exploration Agency (JAXA) [5]. Most of these airborne SAR systems can operate in quad-polarization and interferometric modes. The significant flexibility of the airborne platforms enables extremely dense observations and variable acquisition geometries, e.g., incidence and azimuth angles. These characteristics allow for a better understanding of the surface scattering as well as the temporal behavior, which are essential for the successful development of applications.

The polarimetric L-band imaging SAR (PLIS) is Australia's first L-band polarimetric airborne interferometric SAR system dedicated to scientific research into civilian applications. The main objective of the PLIS system is to provide hydrologic, ecologic, atmospheric, and oceanic researchers with a capability for high temporal and spatial resolution observations over Australia. Compared to other airborne SAR systems [2], the weight

1939-1404 © 2018 IEEE. Personal use is permitted, but republication/redistribution requires IEEE permission.
See http://www.ieee.org/publications_standards/publications/rights/index.html for more information.

of PLIS is significantly lower (~38 kg) allowing integration aboard much smaller and lower-cost aircraft, thus making the SAR capability available to a much wider range of users. Since its first flight in 2010, the PLIS has been used for a range of applications.

The PLIS together with the polarimetric L-band multibeam radiometer was used as an active–passive microwave simulator [6] of NASA's soil moisture active passive (SMAP) mission [7]. Three prelaunch experiments (SMAPEx-1, 2 and 3) [8] and two postlaunch experiments (SAMPEx-4 and 5) [9] were carried out in 2010–2011 and 2015, respectively, for the calibration/validation of the SMAP concept. The data acquired by the PLIS system have been extensively used for testing active–passive soil moisture downscaling algorithms for the SMAP [10]–[12].

By making full use of the flexible acquisition geometries of the PLIS, data from the SMAPEx campaigns also allowed the development of novel algorithms for measuring critical environmental variables. Such algorithms include soil moisture retrieval using polarimetric decomposition [13], evaluation and calibration of surface scattering models [14], [15], vegetation biomass estimation [16]–[18], estimation of vegetation water content [19], [20], and inland water body detection [21].

More applications of the PLIS are expected in the near future, including the development and evaluation of soil moisture retrieval algorithms for the proposed L-band SAOCOM constellation [22], monitoring the effect of bushfires and the subsequent recovery of affected areas throughout Australia [23], and high spatial resolution land use land cover (LULC) mapping. All these applications need an accurate calibration of the PLIS sensor in terms of both polarimetry and radiometry as per the requirements for the various applications provided in [24]. Briefly, the absolute and relative calibration accuracy is required to be better than ±1 dB and ±0.5 dB, respectively. For polarimetric data, additional requirements are that the polarimetric channel balance be better than ±0.4 dB and ±5° in phase, with the crosstalk isolation better than 30 dB [25].

To verify that such criteria have been met, active or passive point targets with large radar cross section (RCS) and known polarimetric characteristics (e.g., trihedrals and transponders) are commonly used. Radiometric calibration factors, polarimetric calibration parameters, and image quality are derived from the impulse response functions (IRFs) of these point targets [26]–[30]. The main challenges of using point targets are as follows:

1) the uncertainty introduced by the interaction with the background;
2) the need to carefully set and maintain their orientation angles;
3) the poor visibility in coarse SAR images (e.g., the 3-km resolution SMAP radar); and
4) their relatively large size compared to the spatial sampling of high resolution SARs.

Alternatively, a uniformly distributed scene (clutter), such as homogeneous dense forests, can be used for calibration; the RCS and polarimetric characteristics of which are either measured by ground-based scatterometers [31] or assumed to satisfy some time-invariant prior-knowledge [28], [30], [32]–[34]. The former is commonly unavailable for a large area while the latter may suffer from uncertainty of the prior-knowledge.

TABLE I
PLIS SYSTEM SPECIFICATION

System Parameter	Value
Frequency	L-Band, 1.26 GHz
Peak transmit power at output of SSPA	30 W
Pulse repetition frequency	Up to 20 kHz
Transmitter duty cycle	< 4%
Pulse width	0.1- 20 µs
Max. bandwidth	30 MHz
Polarization	HH, VV, HV, VH
Beamwidth (H- and E-plane)	~ 51°
Antenna gain	9 dBi
System noise figure	~5.2 dB
Antenna cross polarization	< - 30 dB
Flight height / swath width	Typically 3 km / 2.2 km (15 - 45°)
Measured noise equivalent normalized radar cross-section	< -47 dB m^2/m^2 (10 m range resolution and 3 km flight height)
Typical range spacing	3.75 m
Typical azimuth spacing	2 m

Cross-calibration among different radar systems is another promising approach where airborne SAR observations can be the intermediate step for the calibration of space-based SARs [24]. However, very few studies on this topic have been carried out mainly because of the difference in observation time, radar configuration, and look direction (azimuth and elevation angle). In [31], a ground-based scatterometer was used to calibrate AIRSAR, and different tracks and polarizations of SIR-C/X-SAR were cross-calibrated in [35]. More recently, QuikSCAT and Oceansat-2 were cross-calibrated in [36].

In this paper, the capabilities of the PLIS system and its calibration results during two recent field campaigns (SMAPEx-4 and 5) are presented as a reference for PLIS users. Moreover, the potential for cross-validation/calibration among SAR systems was investigated through a comparison between PLIS and the phased-array L-band synthetic aperture radar 2 (PALSAR-2) data.

II. PLIS SYSTEM

A. System Overview

PLIS was developed in 2010 by ProSensing Inc. to provide high spatial resolution L-band radar observations using a small low-cost aircraft. The weight of the system is about 38 kg, including a Radio Frequency (RF) unit, main and auxiliary dual polarized antenna pairs which can be used separately, a radar data system, and external support components including cables, heaters, and power supply. A detailed description of the PLIS system is provided below (see Table I).

1) *Signal Generation and RF Circuits:* A direct digital synthesizer generates either an unmodulated or linear frequency modulated (LFM) waveform which is then single stage up-converted to RF by mixing with the output from a 1170 MHz phase locked oscillator. For unmodulated waveforms, the pulse width can be varied from 100 ns to 10 μs resulting in a maximum slant range resolution of 15 m. For LFM waveforms the maximum bandwidth

that can be chosen is 30 MHz giving a slant range resolution of 5 m. More commonly a bandwidth of 20 MHz is used giving a slant range resolution of 7.5 m. Subject to the constraint that the duty cycle not exceed 4%, the pulse repetition frequency (PRF) can be varied to 20 KHz allowing unambiguous Doppler measurements up to 10 KHz. When using a 20 KHz PRF the unambiguous range is 7.5 km. To minimize transmitted power leaking into the nearby GPS band a 25 MHz cavity filter has been placed prior to a 30 W peak solid-state amplifier. PLIS also employs an internal calibration loop where the transmit signal can be fed via an attenuator directly to the down-converters prior to the digital receiver.

2) *Antennas:* The main antennas are usually installed beneath the aircraft and consists of a right and left pointing antennas mounted at 30° off nadir. A programmable switching network enables transmission through the right and left pointing antennas to be interleaved. Each antenna is a 2×2 patch array with an $\sim$20 cm aperture, giving a measured one-way beamwidth of $\sim 51°$ and theoretical gain of approximately 7 dBi. A similar auxiliary antenna pair can be mounted with an offset enabling interferometric processing to be undertaken. To avoid detuning, the working temperature of each antenna is maintained at a constant 20 °C using temperature-controlled heater strips.

3) *Polarimetry:* Prior to each antenna there is a two-port network that allows switching the antenna from H to V polarization, thus enabling the full polarization scattering matrix to be estimated on both sides of the aircraft; when the switching is enabled there is a resultant reduction in effective PRF. The cross-polarization isolation has been measured at less than 30 dB.

4) *Radar Data System:* The radar data system consists of a standard server mainboard, a two-channel digital receiver and GPS receiver/timestamp card. The two-channel digital receiver samples the data using two 16-bit digitizers at a sampling rate of 120 M samples/s, with an on-board field-programmable gate array employed to implement I/Q demodulation and decimation filtering. The GPS receiver/timestamp card together with the radar control board is employed to determine the absolute time of acquisition.

5) *External Support Components:* An inertial measurement unit aboard the aircraft platform provides navigation and flight attitude data with a sample rate of 10 Hz. This ensures precise flight track control and are used in the motion compensation during the offline preprocessing stage. In addition, a graphical user interface provides a friendly environment to configure PLIS, and real-time monitoring including raw I/Q voltages, the corresponding power, the filtered pulse power, and the phase after application of the optimal pulse compression filter.

B. Operation and Data Preprocessing

PLIS is operated on a small scientific aircraft. The use of this low-cost aircraft provides great flexibility of the flight altitude and direction, thus allowing mapping with different incidence and azimuth angles. However, it also constrains the stability of the mapping geometry, resulting in the need for precise motion compensation.

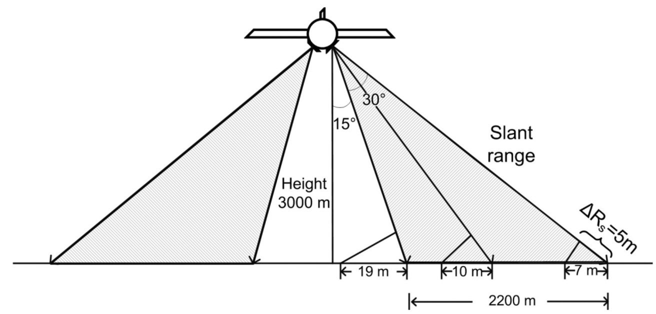

Fig. 1. Schematic of PLIS mapping geometry at a flight height of 3000 m.

The antennas are installed beneath the aircraft with their broadside direction at 30° to nadir. The system has typically been operated at 3000 m altitude with a speed of 75 m/s (maximum 90 m/s); the flying height above ground can be varied from 150 to 3000 m. Operation within this altitude envelope allows better signal-to-noise ratio. However, the large incidence angle variation results in significant change of the crosstrack ground resolution, as shown in Fig. 1, as well as an approximately 8 dB variation across the swath. Nevertheless, PLIS data can be normalized to a specified reference angle by using an incidence angle normalization algorithm [37].

The PLIS supports the acquisition of high resolution imagery with a choice of different polarizations and operation modes, which can have a significant effect on the sample rate. The PLIS sampling rate is based on the recommendations of Gamma Remote Sensing Software, that the PRF be set to sample no slower than one pulse per one-third the effective aperture size in the along-track dimension [38]. The system supports the following operation modes.

1) Single polarization, in which the radar signal with a selected polarization is transmitted by left or right antenna or left then right interleaved and received by the same antenna/s.
2) Dual polarization, in which the transmit polarization is alternated from pulse to pulse with the antenna changing from side to side simultaneously and only the two copolarized channels stored.
3) Quad polarization, in which the transmit signal switches in the order of left vertical polarization (V), left horizontal polarization (H), right V and right H with all four polarization combinations recorded.
4) Single-pass interferometric mode, in which the signal is transmitted in the same order as the quad mode with the backscattered signal received by both the main and auxiliary antennas simultaneously.

The PLIS can also be operated in various resolution modes. The transmitted pulse can be any constant amplitude waveform within the constraints of the transmitter duty cycle ($<4\%$) and the maximum system bandwidth (30 MHz). Fig. 1 shows the typical mapping geometry and the corresponding ground resolutions across the 2.2 km swath given a flying height of 3000 m and a bandwidth of 30 MHz. The preprocessing of PLIS

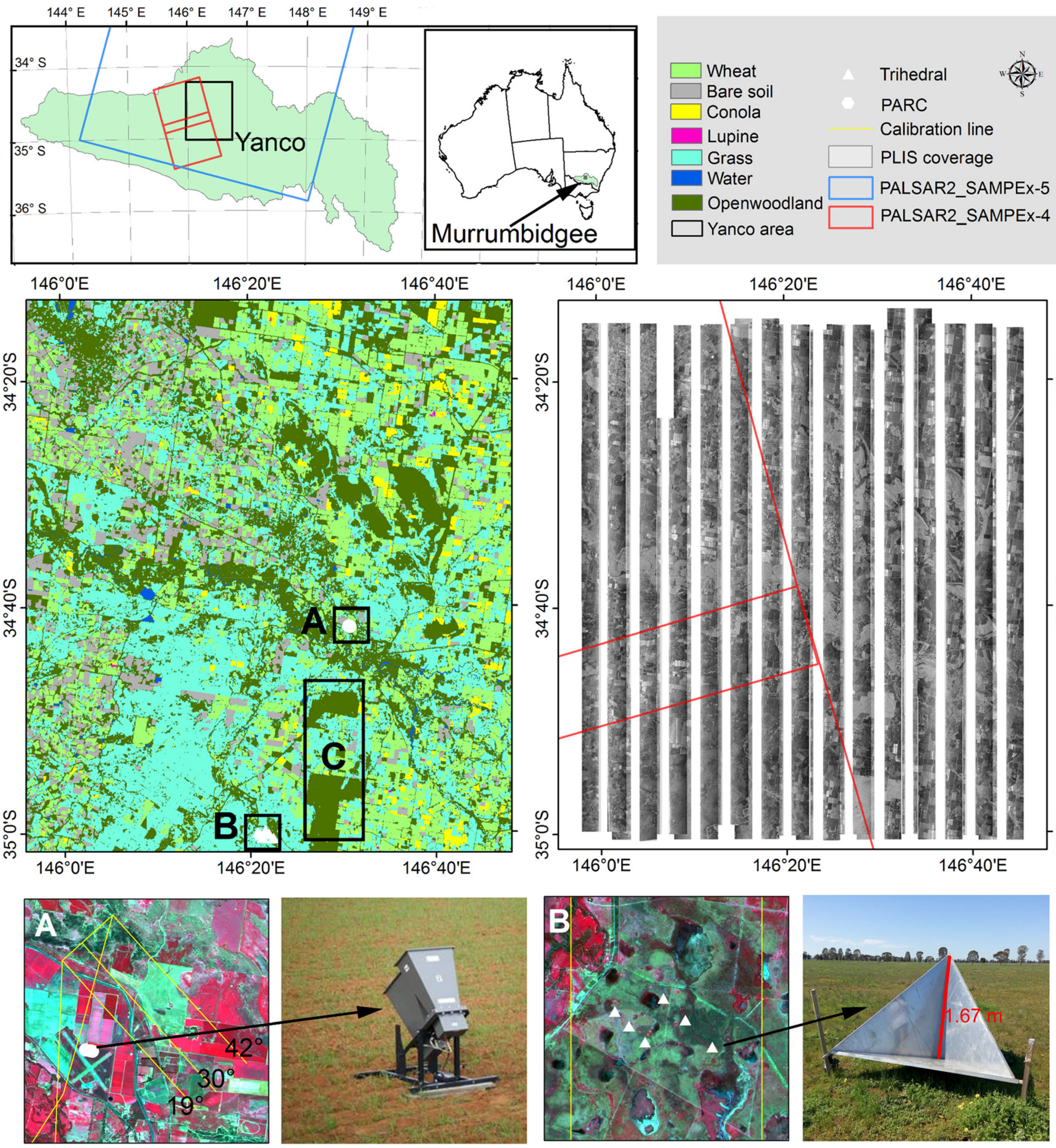

Fig. 2. Calibration sites and flights used in the calibration and validation, as well as the PLIS and PALSAR2 coverage during the SMAPE-4 and -5. The top left shows the location of the Yanco agricultural area and the spatial coverage of PLIS and PALSAR-2 data. The middle left is the land cover map of SMAPEx-5 with the main calibration sites delineated in black rectangles. Areas A and B show the deployment of PARCs and trihedrals for the corresponding calibration flights (the yellow lines in the bottom panel), respectively. Area C includes the forest areas used in the polarimetric calibration. The middle right is an example of PLIS HH data acquired on September 17, 2015.

data is carried out using the Gamma Modular SAR Processor (MSP). The main steps include:

1) extraction and concatenation of a set of overlapping raw files;
2) prefiltering and range compression of raw data;
3) motion compensation of range-compressed data based on the IMU data;
4) range antenna pattern correction; and
5) azimuth compression.

More details can be found in the Gamma MSP documentation [38]. The output of the preprocessing is 16-bits slant-range single look complex (SLC) data. The slant-range spacing is ~3.75 m given an analog to digital converter sampling frequency of 40 MHz and the prefiltered azimuth spacing is typically on the order of 2 m. However, a finer sampling in azimuth is possible (e.g., 0.5 m) by applying different prefilter parameters.

III. Calibration and Evaluation

A. *Experiments and the Calibration Site*

As aforementioned, the PLIS has been used in five SMAPEx campaigns. The detail of SMAPEx-1, 2, and 3 as well as a brief introduction to the corresponding calibration is provided in [8] and [18]. Similar to these three campaigns, two types of targets were used for calibration in SMAPEx-4 and 5. One is a large forest area (see area C in Fig. 2) which was used in the polarimetric calibration on a daily basis. The other was artificial reflectors including trihedral passive radar calibrators (PRCs)

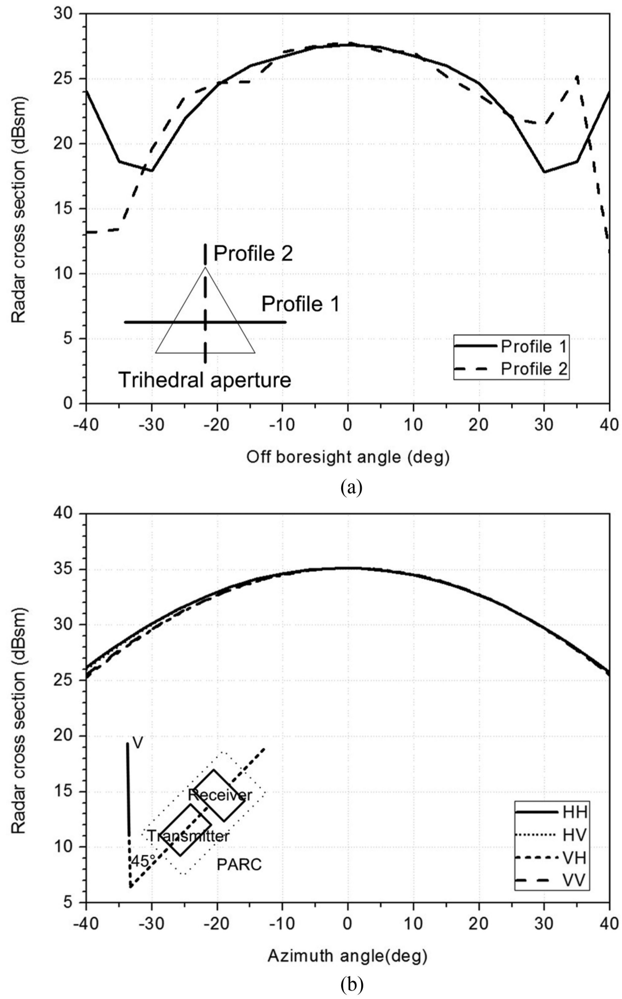

Fig. 3. RCS patterns of the (a) trihedral and (b) PARC for L-band.

otherwise known as corner reflectors, and polarimetric active radar calibrators (PARCs).

Specifically, six metallic trihedrals with a leg length (l) of 1.665 m were deployed at a single calibration site located in a flat, uniformly grazed area (see area B in Fig. 2). The theoretical RCS of these targets is 27.5 dBsm, given by $4\pi l^4/3\lambda^2$ with λ being the wavelength. Fig. 3(a) shows the RCS pattern along the azimuth and elevation directions. The trihedrals were uniformly distributed across the PLIS swath, with their symmetric axis parallel to the direction of incident signal. The local incidence angle at the six trihedrals was 15°, 21°, 27°, 33°, 39°, and 45°, respectively, in SMAPEx-4, while the 15° trihedral was moved to a location with an incidence angle of 51° in SMAPEx-5 to represent the far edge beam.

A PARC aligning to receive 45° linear polarization and retransmit −45° linear polarization was also deployed within the Narrandera airport grounds (see area A in Fig. 2) for calibration during the SMAPEx-4 and -5 campaigns. The theoretical polarimetric response of this PARC is

$$S = \begin{bmatrix} -1 & -1 \\ 1 & 1 \end{bmatrix} \tag{1}$$

where the first row denotes the normalized amplitude of HH and HV, and the second row are that of VH and VV. The sign of each element represents the relative phase. The RCS of the PARCs is ~35.1 dBsm, with its dependence on azimuth angle, as shown in Fig. 3(b). The temperature of the PARC antennas was recorded to determine the real-time RCS, using a carefully measured temperature-RCS look up table. The response of this PARC is expected to independently provide polarimetric accuracy estimates of the calibrated data [26]. Calibration flights over the PARC were carried out as a "calibration circuit" consisting of three overpasses, with the PARC falling toward the far edge of run 1 (42° incidence angle), in the center (30° incidence angle) of run 2, and toward the near edge of run 3 (19° incidence angle), respectively. The calibration circuits were undertaken only at the start and end of the airborne campaigns.

B. Calibration

The calibration of PLIS data included two steps, taking the preprocessed 16-bit slant-range SLC as the following input.

1) *Polarimetric Calibration:* The *a posteriori* method based on a distributed target as proposed in [33] was used to estimate crosstalk parameters (u, v, w, z) and one of the channel imbalance parameters α. The distortion model relating the actual $([s_{\text{hh}}, s_{\text{hv}}, s_{\text{vh}}, s_{\text{vv}}]^T)$ and observed $([O_{\text{hh}}, O_{\text{hv}}, O_{\text{vh}}, O_{\text{vv}}]^T)$ scattering matrixes, and derivation of the corresponding calibration matrix can be found in [33]. Briefly, this algorithm iteratively updates u, v, w, z and α, with an initial guess of zero crosstalk using data over a distributed area, e.g., dense forest. The trihedrals were then used to estimate the other imbalance parameter k denoting the reception imbalance between HH and VV. Finally, the estimated crosstalk and imbalance parameters were employed to correct the observed SLC data

$$\begin{bmatrix} s_{\text{hh}} \\ s_{\text{hv}} \\ s_{\text{vh}} \\ s_{\text{vv}} \end{bmatrix} = \begin{bmatrix} k\alpha & u\alpha^{-1} & w\alpha & vwk^{-1}\alpha^{-1} \\ zk\alpha & \alpha^{-1} & wz\alpha & wk^{-1}\alpha^{-1} \\ uk\alpha & w\alpha^{-1} & \alpha & vk^{-1}\alpha^{-1} \\ uzk\alpha & u\alpha^{-1} & z\alpha & k^{-1}\alpha^{-1} \end{bmatrix} \begin{bmatrix} O_{\text{hh}} \\ O_{\text{hv}} \\ O_{\text{vh}} \\ O_{\text{vv}} \end{bmatrix}. \tag{2}$$

2) *Absolute Radiometric Calibration:* The well-known integral method based on trihedrals [27] was used to estimate the absolute calibration coefficient. Fig. 2 illustrates the definition of point target area A_{pnu} and background area A_{nu} for the purpose of extracting the point energy in this study. The energy of the trihedrals was estimated as

$$\varepsilon_p = \left(\sum_{A_{pnu}} I_{ij} - \frac{A_{\text{pnu}}}{A_{\text{nu}}} \sum_{A_{nu}} I_{ij} \right) \cdot \delta_a \cdot \delta_r / \sin\theta \tag{3}$$

where I_{ij} is the intensity of the pixel ij and θ is the incidence angle. δ_a and δ_r are the azimuth and range spacing, respectively. The absolute calibration factor from a trihedral (C_{tri}) can thus be estimated using $C_{\text{tri}} = \sigma/\varepsilon_p$ where σ is the theoretical RCS of the trihedral. Six trihedrals were deployed for different range bins and accordingly C_{tri} could be calculated for different range bins for each calibration flight. The average (C) of all calibration

TABLE II
PLIS AND PALSAR-2 IMAGES USED IN THE CROSS-VALIDATION

	SMAPEx-4 scenario		SMAPEx-5 scenario	
	PLIS	PALSAR-2	PLIS	PALSAR-2
Observation mode	Stripmap	ScanSAR	Stripmap	Stripmap FBD
Day of year (UTC)	130	132	266	267
Overpass time offset	~ 32 hours		~ 19 hours	
Incidence angle	15° - 50°	36.5° - 43.5°	15° - 50°	31.5° - 34.5°
Polarization	HH+VV+HV +VH	HH+HV	HH+VV+HV +VH	HH+HV
Orbit/direction	North-South, South-North	Descending (inclination: 97.9º)	North-South, South-North	Ascending (inclination: 97.9º)
Spatial resolution	10 m	100 m	10 m	10 m
Soil moisture* (m^3/m^3)	0.172	0.143	0.107	0.105

*Average soil moisture is estimated from OzNet and ground sampling.

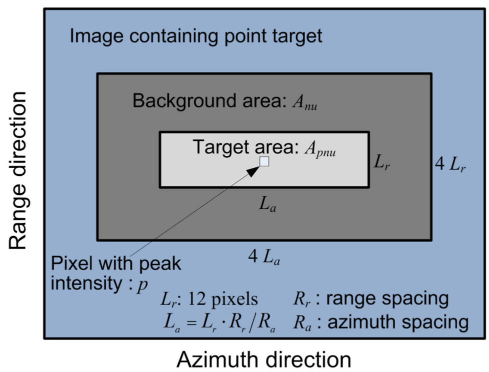

Fig. 4. Definition of point target area and background area for extracting the response of a point target. The range and azimuth spacing are 3.75 and 2 m, respectively.

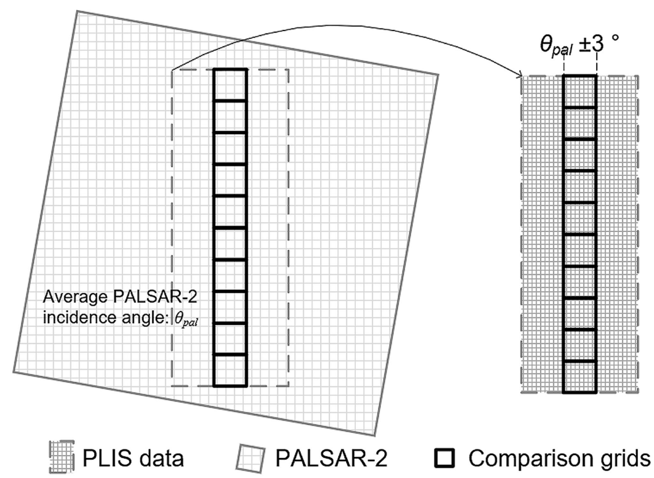

Fig. 5. Schematic of PLIS and PALSAR-2 comparison. The grid cell size in azimuth and look direction is the same, but the real ground size ranges from 500 to 750 m for different PLIS strips because of the variation of ground range spacing.

coefficients of a campaign were used to provide a single set of calibration parameters for all observations throughout the campaign. The absolute calibrated σ^0 (dB) for each pixel was then calculated

$$\sigma^0 = 10 \log_{10}(s \cdot s^*) - C \tag{4}$$

where s^* is the complex conjugate of the polarimetric calibrated SLC s. The C of SMAPEx-4 were −37.74 dB (left) and −37.69 dB (right), respectively, while they were −37.59 dB (left) and −37.79 dB (right) for SMAPEx-5. The stability of C_{tri} in the range direction and time for each campaign is provided below in terms of the residual RCS $(C - \text{C}_{\text{tri}})$ after calibration.

C. Evaluation Over Point Targets

The PLIS 3-dB resolution, the peak-to-side lobe ratio (PSLR), and the integrated side lobe ratio (ISLR) were estimated using the IRFs of the PARCs. Specifically, the target area in Fig. 4 was interpreted into 1024 × 1024 pixels using the fast Fourier transform. Two one-dimensional profiles (azimuth and range) through the peak pixel were then used to estimate these quantities. In addition, the polarimetric matrix of the PARC was used to provide independent evaluation of the calibrated data. The integration method was also used to estimate the amplitudes of the PARC by simply replacing the intensity with amplitude in (3), while the phase of the peak pixel was treated as that of the PARC. The residual radiometric and polarimetric error over trihedrals after calibration was estimated to show the quality of the calibrated data in terms of accuracy and stability in time and space, though they had been used in the estimation of *k* and *C*.

D. Cross-Validation With PALSAR-2

Two PALSAR-2 images acquired during the SMAPEx-4 (May 1–22,2015) and −5 (September 7–27) experiments were available for cross-validation. The PLIS data with a minimum time offset (32 and 19 h, respectively) with respect to the PALSAR-2 data were selected. The details of the data used in comparison are given in Table II with their spatial coverage shown in Fig. 2. Georegistration of both the PALSAR-2 and PLIS images was carried out taking the Landsat-8 operational land imager(OLI) image acquired on September 30, 2015 as reference. The spatial miss-registration error was less than 1 pixel (10 m) for PLIS and PALSAR-2 Stripmap images. PALSAR-2 ScanSAR image showed a larger spatial uncertainty (70 m) because of the difficulty in identifying point targets during georegistration. sused

Since PLIS and PALSAR-2 have different incidence angles and spatial resolutions, they were resampled onto a coarser grid for cross-validation (see Fig. 5). Specifically, the average incidence angle (θ) of PALSAR-2 within the PLIS coverage was calculated, with grids generated to include the PLIS pixels whose

TABLE III
PLIS CALIBRATION ACCURACY AND ITS COMPARISON WITH ANOTHER TWO L-BAND AIRBORNE SAR SYSTEM

	Items	PLIS	Pi-SAR-L2 [5]	UAVSAR [39, 40]	Requirement [24, 25]
3dB resolution	Azimuth (m)	2.07 ± 0.12	1.01 ± 0.25	0.94	
	Range (m)	5.97 ± 0.28	1.8 ± 0.06	2.53	
Side lobe	PSLR in azimuth (dB)	-16.13 ± 3.19	-9.05 ± 3.42	Azimuth Tx: -11*	
	ISLR in range (dB)	-12.12 ± 2.51	-9.05 ± 3.42	Azimuth Ty: -20*	
	PSLR in range (dB)	-16.07 ± 2.90	-7.04 ± 1.26	Range: -30*	
	ISLR in azimuth (dB)	-11.04 ± 2.65			
Polarimetric calibration	Amplitude imbalance (dB)	0.17 ± 0.15; 0.22 (RMS)	0.09 ± 0.10	0.17 (RMS)	0.4
	Phase imbalance (°)	3.87 ± 2.86; 4.81 (RMS)	1.368 ± 2,142	5.3 (RMS)	5
	Crosstalk (PRC) (dB)	-27.58 ± 1.02	<-32	-30	-30
	Crosstalk (nature target) (dB)	-30.55 ± 1.01	-38.62		
Radiometric calibration (dB)		0.58 (RMS); 0.82 (1 sigma)	1.16 (1 sigma)	0.7 (RMS)	1
Comparison with PALSAR-2	RMSD with ScanSAR (dB)	2.47 (HH);1.92 (HV)			
	RMSD with Stripmap (dB)	1.29 (HH); 1.01(HV)			

PSLR and ISLR are peak-to-side-lobe-ratio and integrated-side-lobe-ratio. A ± B represents an average of A and a standard deviation of B. * denotes the design requirement

incidence angles fall within $\theta \pm 3°$. These grid cells have the same size in the azimuth and range directions. It is worth noting that the ground resolution in the range direction is different, resulting in different sizes of the grid cells (500–750 m) at different incidence angles. The ensemble mean of PLIS and PALSAR-2 for each grid was calculated for further comparison. Four metrics, i.e., correlation coefficient (R), bias, root-mean-squared difference (RMSD) and unbiased RMSD (ubRMSD) were used to represent the agreement between PLIS and PALSAR-2. The ubRMSD is defined as

$$\mathrm{ubRMSD} = \sqrt{\sum_{i}^{N} \left(x_i - y_i - (\mu_x - \mu_y)\right)^2 / N} \tag{5}$$

where x_i and y_i are the *i*th grid of PLIS and PALSAR-2, *N* is the number of grid cells in comparison. μ_x and μ_y are the mean of *x* and *y*, respectively. In addition, land cover maps of SMAPEx-4 and 5 derived from Landsat-8 OLI images were used to analyze the effect of LULC on cross-validation/calibration.

IV. Evaluation Results

A. Calibration Accuracy Over Point Targets

A summary of PLIS image quality parameters is given in Table III. The estimated azimuth and range 3-dB resolutions were 2.07 and 5.97 m, respectively. The average PSLR were −16.13 dB in azimuth and −16.07 dB in range, the latter of which can be further improved using data specific least-mean-square filter coefficients in the range compression, but at the cost of broadening point target responses.

Fig. 6(a) shows the difference between observed and theoretical RCS (residual error) over all trihedrals of SMAPEx-4. In general, this difference was less than 0.5 dBsm for most of the trihedrals which satisfies the absolute calibration accuracy requirement [24]. A satisfactory balance between HH and VV phase was also observed with an RMSD of 0.17 dBsm. In addition, no clear pattern of residual RCS could be found with respect to the incidence angle, although trihedrals with incidence angles of 23° and 27° had negative residuals while positive residuals were observed over others. This can be partly explained by the limitation of the trihedral approach and the integral method used to extract its RCS. The interaction between trihedral and background is well known to introduce uncertainty in the estimation of the RCS, which cannot be removed by the integral method [31], [41]. This uncertainty can vary from trihedral to trihedral because of the variation of the background over the time and space domain. The variation in time series can in turn partly explain the variation of the RCS of trihedrals at the same incidence angle. The instability of the small aircraft platform from day to day (e.g., slight changes of flight track and observation geometry) is another explanation for these phenomena. Fig. 6 also includes the copolarized phase difference (HH/VV) of all trihedrals, which should be close to zero. The copolarized phase difference of less than 5° achieved in almost all cases satisfies the accuracy requirement in phase. It is worth noting that as all trihedrals were involved in the polarimetric calibration (estimation of the imbalance of HH and VV), the near zero phase difference was expected with further validation using the PARC required, as presented later.

Fig. 6(b) shows the results of SMAPEx-5, which are similar to those observed for SMAPEx-4. The residual RMSE of HH and VV were 0.62 and 0.68 dBsm, respectively. The RMSD between HH and VV was 0.21 dBsm. Notably, the trihedral deployed at the outer edge of the PLIS swath during SMAPEx-5 did not have much variation from the remaining ones, suggesting that the PLIS data from far range bins was also of high quality. The negative difference between the observed and theoretical RCS of the 23° trihedral in SMAPEx-4 was not found in SAMPEx-5, refuting any suggestion of angular instability of the PLIS. The small difference (<0.2 dB) between the SMAPEx-4 and -5 absolute calibration coefficient *C* confirmed the sensor stability of sensor between campaigns. The short-term relative calibration accuracy of PLIS data is reflected in Fig. 6(c). The largest day to day difference with respect to the theoretical cross section were 0.56 dBsm observed between DOY 126 and 134, and 0.58 dBsm observed between DOY 252 and 257, for SAMPEx-4 and 5, respectively, which slightly exceed the target calibration requirements of <0.5 dB [24]. The instability of trihedral orientation and aircraft platform mapping geometry may be the main reason for this larger short-term variation. Fig. 6(d) shows the corresponding averaged crosstalk estimated from trihedrals, which were 2–4 dB greater than the calibration requirements

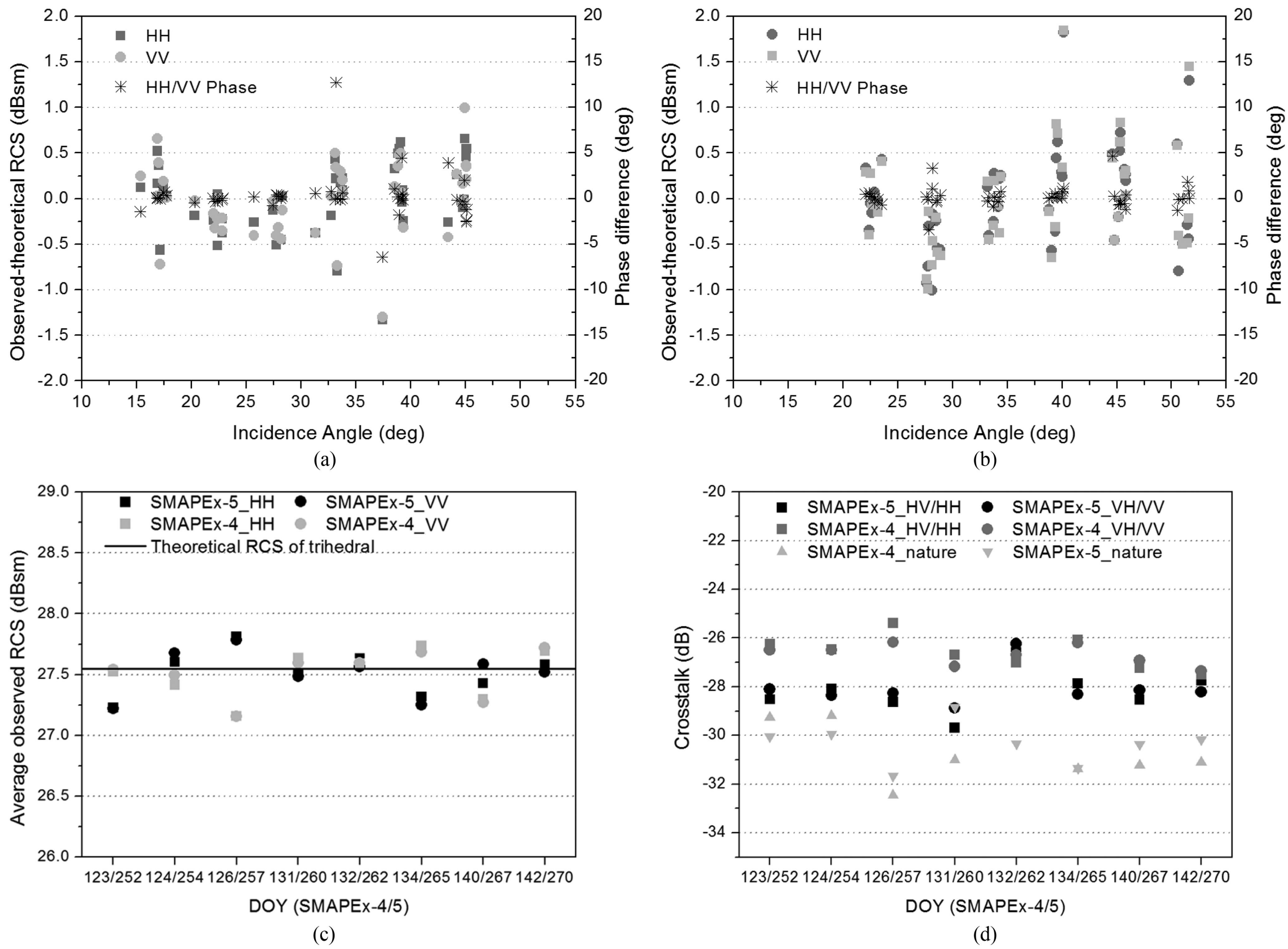

Fig. 6. Response of trihedral PRCs after calibration. (a) and (b) RCSs and copolarized phase differences of all trihedrals during SMAPEx-4 and 5, respectively. (c) and (d) Time series average RCS of trihedrals and the averaged crosstalk estimated from trihedrals and forest, respectively.

of −30 dB. This was mainly caused by the stronger multiple scattering between the trihedrals and ground surface compared to those directly from ground. The difference in ground response under the trihedrals between two field campaigns may be the main reason for the higher crosstalk in SMAPEx-4. The crosstalk (the correlation of HV and HH) estimated from a distributed area (i.e., the forest area *C* in Fig. 2), was on the order of −30 dB which is similar to the calibrated UAVSAR data [39] using the same polarimetric calibration method [33].

Fig. 7 shows the channel imbalance of PARCs after calibrating the SMAPEx-5 data. The PARC with local incidence angle of 42° could not be identified in the image of September 27, 2015 (DOY 270) and thus was not included. In general, the calibrated PLIS data achieved satisfactory accuracy in both amplitude and phase. The amplitude imbalance of most channels at the three different incidence angles was less than ±0.4 dB. The observed phase differences among different polarizations are very close to the theoretical ones (i.e., 0° for HH/HV and VH/VV, and 180° for the rest). The average phase imbalance was 3.87°. No clear angular pattern was observed despite the large variation of amplitude ratio and phase difference among the different incidence angles.

To demonstrate the quality of the calibrated PLIS data, examples of Freeman–Durden polarimetric decomposition [42] are analyzed in Fig. 8 where the dihedral, volume, and surface power in dB are set to red, green, and blue, respectively. Fig. 8(a) and (b) shows results of an urban area and dense forest area. Significant difference was observed between the forest and urban area with the dominant components being the volume and dihedral scattering, respectively. Strong volume scattering was also observed in some parts of the urban area (yellow patches). This was mainly caused by dense trees near buildings. The field within the black boundary [see Fig. 8(b)] was bare soil with a significant row structure perpendicular to the radar look direction, and thus dihedral scattering was the dominant component. Fig. 8(c)–(e) shows the decomposition results over agricultural areas at three different times, the beginning (May 3, 2015) and end (September 24–27, 2015 irrigated and nonirrigated) of the winter wheat growing cycle. In May, almost all fields were bare and thus the surface component (blue shades) was predominant. In September, some fields were covered with fully developed dry wheat characterized by increased dihedral and volume scattering contributions. Irrigation was carried out in the fields with white boundary between September 24–27th, resulting in an abrupt increase in all three mechanisms because of the sudden supplement of water in both soil surface and vegetation.

It's worth noting that the actual incident radar signal is not strictly perpendicular to the aperture of the PARCs and trihe-

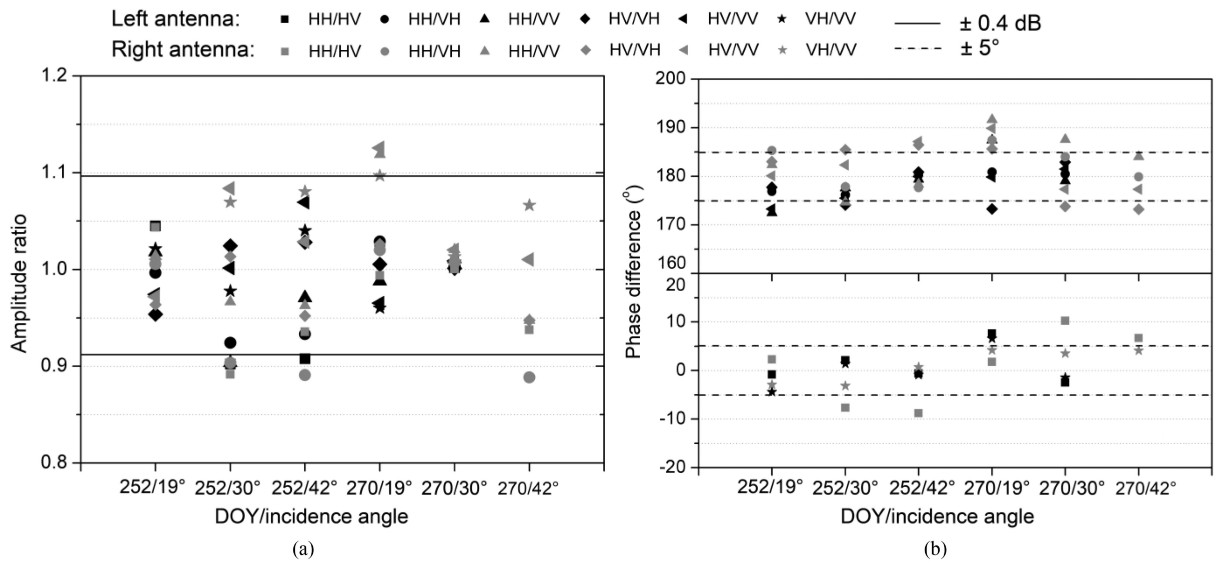

Fig. 7. (a) Amplitude and (b) phase differences of the polarimetrically calibrated PLIS data from PARCs.

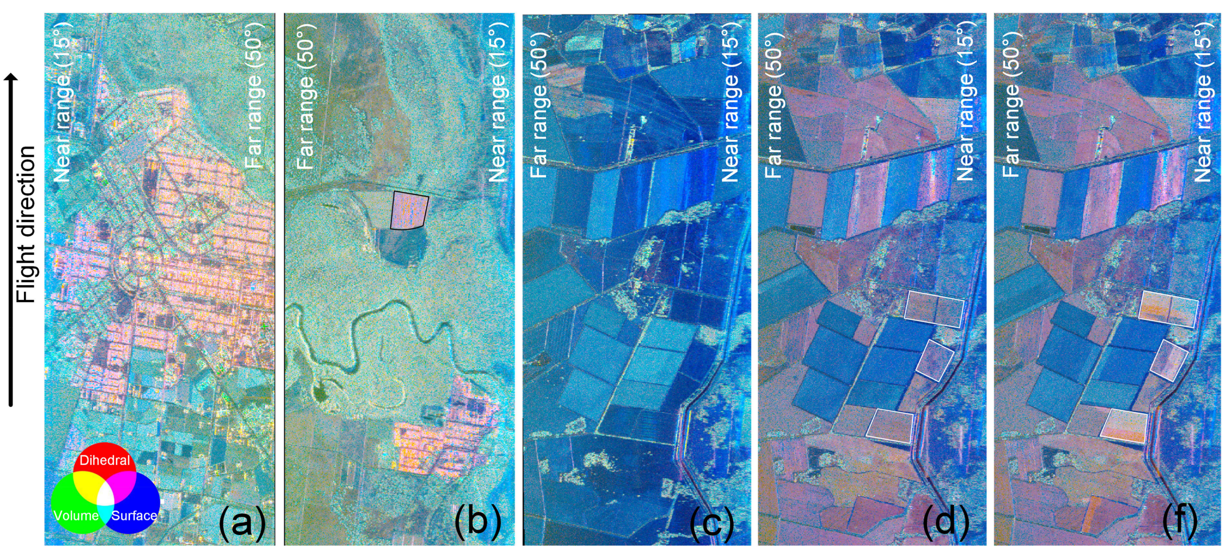

Fig. 8. RGB image of the Freeman–Durden decomposition powers in dB where red, green, and blue are dihedral, volume and surface component, respectively. (a) and (b) Results over an urban and forest area, respectively. (c)–(f) Results of May 3rd, September 24–27 of an agricultural area where the irrigated fields were delineated with white boundaries.

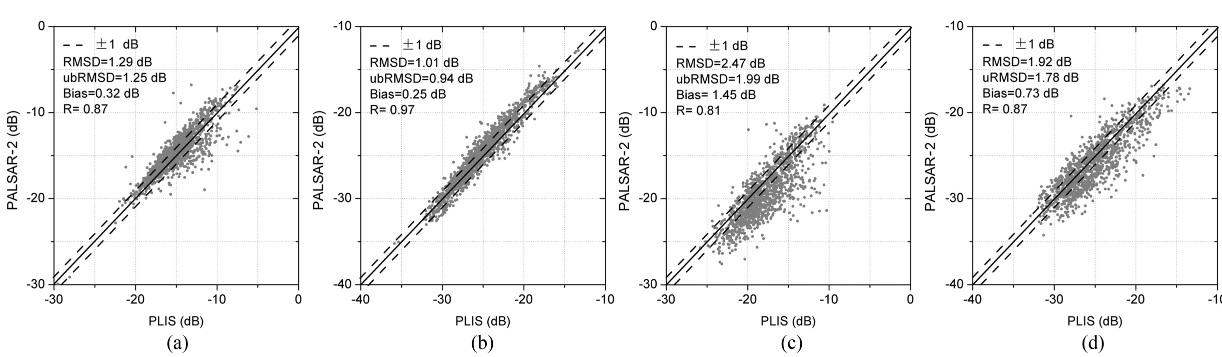

Fig. 9. Comparison of PLIS and PALSAR-2 backscattering coefficient in dB. (a) and (b) HH and HV for SMAPEx-5 (PLIS and PALSAR-2 Stripmap) respectively while (c) and (d) are HH and HV for SMAPEx-4 (PLIS and PALSAR-2 ScanSAR).

drals. The angle offsets, which were less than 3° as shown in Fig. 6(a) and (b), can introduce uncertainty in estimating the scattering characteristics of these targets. Fortunately, both the trihedrals and PARCs have a very wide beamwidth (see Fig. 3), meaning that the effect of the observed offsets on the RCS of the trihedral and PARC were less than 0.1 dB with negligible channel imbalances. However, the angle offsets can also introduce a small copolarized phase difference (<3°) for the trihedral at L-band [43], [44]. With respect to the PARC, the phase of all polarizations was retained and thus the phase differences are independent on the angle offsets. Nonetheless, the interaction between calibration targets and background can be different for different incidence angle, introducing unclear uncertainty.

B. Comparison of PLIS and PALSAR-2

The PLIS data shows a high agreement with the PALSAR-2 Stripmap image, with R better than 0.87 and RMSD better than 1.25 dB for both channels (see Fig. 9). The HV polarization showed the highest agreement with an ubRMSD of 0.94 dB. The biases between PLIS and PALSAR-2 Stripmap for HH and HV were 0.32 dB and 0.25 dB, respectively. This difference may be related to uncertainties in the calibration of both sensors, or a small drift between the PLIS and PALSAR-2 Stripmap, as soil moisture was nearly constant between the two acquisitions (see Table II).

The agreement between PLIS and PALSAR-2 ScanSAR is not as good (see Fig. 9). The RMSD for HH and HV were 2.47 and 1.92 dB, nearly double compared to those observed between PLIS and PALSAR-2 Stripmap. The average HH and HV measured by PLIS were, respectively, 1.45 and 0.73 dB larger than those of PALSAR-2 ScanSAR image. Such large positive biases can be partly explained by the change of soil moisture between the two acquisitions, which decreased from 0.17 to 0.14 m^3/m^3 during the overpass of PLIS and PALSAR-2. This difference in soil moisture is predicted to result in a decrease in backscattering coefficient of 0.5 and 0.6 dB for HH and HV, respectively; simulated using the integration equation model given a root mean square height of 1 cm and a correlation length of 10 cm. In addition, the relatively large geometric uncertainty of the PALSAR-2 ScanSAR [30] can also introduce large uncertainties, especially for areas with high spatial heterogeneity. Fig. 10 shows the relationship between R of PLIS and PALSAR-2 and spatial homogeneity, where homogeneity is described as the fraction of the dominant land cover. The R of PLIS and PALSAR-2 ScanSAR gradually increased as the spatial heterogeneity decreased, while no clear tendency was observed for the comparison of PLIS and PALSAR-2 Stripmap. This is reasonable because the spatial heterogeneity itself does not introduce uncertainty into the comparison of two well spatially located images. In other words, the effect of the spatial registration error on the comparison is more significant over a heterogeneous area.

The impact of land cover type and azimuth difference between the two sensors is further given in Table IV. Only grid cells with a high spatial homogeneity (where the fraction of dominant land cover type was >80%) were used to eliminate the potential influence of georegistration error. Since the PALSAR-2

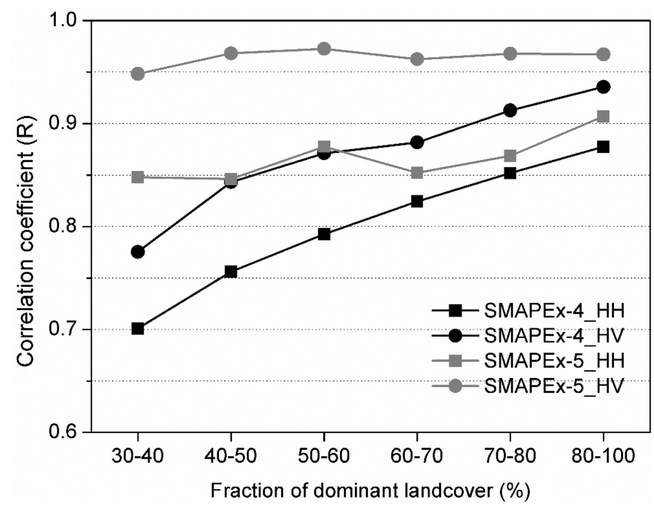

Fig. 10. Relationship between the correlation coefficient and spatial heterogeneity.

TABLE IV
COMPARISON OF PLIS AND PALSAR2 OVER DIFFERENT LANDCOVER TYPES AND LOOK DIRECTIONS

	HH		HV	
PLIS look direction	East-West	West-East	East-West	West-East
SMAPEx-4 scenario				
Bare soil	2.71(0.53)	2.53(0.63)	2.77(0.42)	2.05(0.60)
Wheat	-	-	-	-
Grass	1.42 (0.82)	1.54(0.80)	1.53(0.78)	1.38(0.81)
Forest	**1.34 (0.96)**	**1.17(0.95)**	**1.22(0.95)**	**1.02(0.95)**
Open woodland	1.37 (0.89)	1.47 (0.92)	1.48(0.76)	1.02(0.97)
SMAPEx-5 scenario				
Bare soil	2.23 (0.59)	1.33(0.83)	1.27(0.82)	0.76(0.95)
Wheat	0.91 (0.88)	1.05 (0.91)	**0.74(0.98)**	**0.58(0.99)**
Grass	**0.74 (0.91)**	**0.63 (0.91)**	0.79(0.95)	0.70(0.98)
Forest	-	-	-	-
Open woodland	1.63 (0.71)	1.40 (0.51)	1.09(0.94)	0.93(0.94)

Values in bold indicate the lowest RMSD among different landcover types. A(B) represents a root mean square difference of A and a correlation coefficient of B. Only the grids whose fractions of dominant landcover type were >80% were included.

Stripmap only covered the south-west part of the SMAPEx-5 area (see Fig. 2), less than ten homogeneous forest grid cells were achieved and thus comparison over forest was not included in Table IV. In addition, a large bare soil area in SMAPEx-4 was covered by milk-stage wheat in SMAPEx-5, and thus the comparison over wheat was included in the SMAPEx-5 scenario.

In the SMAPEx-4 scenario, PLIS and PALSAR-2 ScanSAR had much higher RMSD over bare soil than over grass, forest and open woodland. The highest agreement was observed over forest with RMSD of 1.17 dB for HH and 1.02 dB for HV. The smallest RMSD were all achieved when the PLIS observed from west to east. Note that the look direction of PALSAR-2 is also nearly west to east (the inclination of satellite platform is ~97.9 °), indicating that azimuth direction had an impact on the backscatter observations. The impact of look direction for PLIS also varied for different landcover types, resulting in the largest RMSD over bare soil followed by open woodland, grass, and forest. This is consistent with the fact that uniform grass and forest is nearly azimuth symmetric to radar remote sensing, while bare soil, especially with row structures, commonly has different backscattering behavior for different azimuth angles. Similar results were observed in the SMAPEx-5 scenario. The highest agreement was achieved over grass for HH and over wheat for HV, with RMSD less than 0.65 dB and R larger than 0.9. The largest RMSD and lowest R were observed over the bare soil, when PLIS look direction was not aligned to that of PALSAR-2.

V. Conclusion

The stability, accuracy, and image quality of PLIS data was comprehensively evaluated using two airborne campaigns (SMAPEx-4 and 5). The radiometric accuracy (RMSE) was found to be better than 0.65 dB over trihedral PRCs, a slightly improvement when compared to the calibration results of SMAPEx-1, 2, and 3 (the difference between observed and theoretical PRC cross section was on average 0.93 dB) [8]. Short-term stability of PLIS data was confirmed based on the observations acquired during SMAPEx-4 and -5 experiments (a half-year period). When comparing with SMAPEx-3 (2011) and -4 (2015), a shift in C of 1.7 and 0.3 dB for the left and the right antennas was observed, respectively, suggesting a reasonable long-term stability of the PLIS instrument [8]. The imbalance of different channels was 0.17 ± 0.15 dB and $3.87 \pm 2.86°$ over PARCs. The residual HH and VV imbalance over trihedrals after calibration was 0.04 ± 0.05 dB and $0.86 \pm 1.49°$; the former is slightly larger than the near zero amplitude imbalance of SAMPEx-1, 2, and 3. The residual crosstalk estimated from distributed targets was on the order of -30 dB.

The calibration results are close to those observed for other L-band airborne SAR systems (see Table III), i.e., NASA UAVSAR [39] and JAXA Pi-SAR-L2 [45], which meet the accuracy requirements for the various applications listed in [24] and references therein, including age of lava flows classification, ice classification and motion monitoring, vegetation mapping/monitoring, wind speed monitoring over ocean, and soil moisture retrieval.

PLIS / PALSAR-2 cross-validation confirmed the calibration accuracy of the PLIS data over various land cover types and the potential cross-calibration of SAR systems as follows:

1) High correlation ($R > 0.8$) between PLIS and PALSAR-2 backscattering coefficients was observed for both ScanSAR and Stripmap images. However, the comparison of PLIS and PALSAR-2 ScanSAR showed larger RMSD and lower R than that of PLIS and PALSAR-2 Stripmap, which was ascribed to the change of surface conditions during the acquisitions of images and the uncertainty of the ScanSAR geometric accuracy. These are also the main challenges in the cross-validation or cross-calibration between different sensors. The latter has been confirmed to be partly removed by selecting a uniform area. Alternatively, comparing images with a coarser grid resolution is also expected to eliminate the influence of spatial miss-registration, but this may be impractical for airborne SAR and ground-based scatterometer, because of the narrow swath featuring the same incidence angle. Since L-band SARs are very sensitive to the change of soil moisture between overpasses, an investigation of soil moisture variation is necessary before cross-calibration between different L-band SARs observations on different dates.
2) The agriculture area is hardly a Lambertian target and thus the angular behavior of backscattering coefficients is unclear. The PLIS data used in the comparison were within $\pm 3°$ of the average incidence angle of PALSAR-2 data. This may have introduced uncertainties in the cross-validation which could not be determined in this study. With respect to the effect of radar look direction difference, the results have confirmed that over homogenous grass, wheat and forest grid cells, the results are insensitive to the azimuth difference between sensors.
3) The PLIS data had a high agreement with PALSAR-2 Stripmap over homogeneous grassland grid cells for both channels (RMSD < 0.8 dB and $R > 0.9$). The backscattering coefficient of grassland is commonly several dB lower than that of dense forest and wheat, making it an effective cross-calibration target to reflect the accuracy of low backscattering observations.

Acknowledgment

The authors would like to thank the reviewers for their very detailed comments that helped improving the quality of this paper. The authors also acknowledge the scholarships awarded by Monash University and China Scholarship Council (CSC) to support L. Zhu's Ph.D. research. The PALSAR data was provided by JAXA under the framework of the 6th Research Announcement for ALOS-2.

References

[1] "Pulsed Doppler radar methods and apparatus," US Patent US3196436A, 1965.
[2] K. Ouchi, "Recent trend and advance of synthetic aperture radar with selected topics," *Remote Sens.*, vol. 5, no. 2, pp. 716–807, 2013.
[3] P. A. Rosen *et al.*, "UAVSAR: A new NASA airborne SAR system for science and technology research," in *Proc. 2006 IEEE Conf. Radar*, 2006, pp. 22–29.
[4] R. F. Rincon, M. A. Vega, M. Buenfil, A. Geist, L. Hilliard, and P. Racette, "NASA's L-band digital beamforming synthetic aperture radar," *IEEE Trans. Geosci. Remote Sens.*, vol. 49, no. 10, pp. 3622–3628, Oct. 2011.
[5] M. Shimada, N. Kawano, M. Watanabe, T. Motooka, and M. Ohki, "Calibration and validation of the Pi-SAR-L2," in *Proc. Asia-Pac. Conf. Synthetic Aperture Radar*, Tsukuba, Japan, 2013, pp. 194–197.
[6] X. Wu, J. P. Walker, C. Rüdiger, R. Panciera, and D. A. Gray, "Simulation of the SMAP data stream from SMAPEx field campaigns in Australia," *IEEE Trans. Geosci. Remote Sens.*, vol. 53, no. 4, pp. 1921–1934, Apr. 2015.
[7] D. Entekhabi *et al.*, "The soil moisture active passive (SMAP) mission," *Proc. IEEE*, vol. 98, no. 5, pp. 704–716, May 2010.
[8] R. Panciera *et al.*, "The soil moisture active passive experiments (SMAPEx): Toward soil moisture retrieval from the SMAP mission," *IEEE Trans. Geosci. Remote Sens.*, vol. 52, no. 1, pp. 490–507, Jan. 2014.
[9] N. Ye *et al.*, "Towards validation of SMAP: SMAPEX-4 &-5," in *Proc. 2016 IEEE Int. Geosci. Remote Sens. Symp.*, 2016, pp. 3469–3472.
[10] X. Wu, J. P. Walker, N. N. Das, R. Panciera, and C. Rüdiger, "Evaluation of the SMAP brightness temperature downscaling algorithm using active–passive microwave observations," *Remote Sens. Environ.*, vol. 155, pp. 210–221, 2014.

[11] X. Wu, J. P. Walker, C. Rüdiger, and R. Panciera, "Effect of land-cover type on the SMAP active/passive soil moisture downscaling algorithm performance," *IEEE Geosci. Remote Sens. Lett.*, vol. 12, no. 4, pp. 846–850, Apr. 2015.
[12] X. Wu, J. P. Walker, C. Rüdiger, R. Panciera, and Y. Gao, "Intercomparison of alternate soil moisture downscaling algorithms using active-passive microwave observations," *IEEE Geosci. Remote Sens. Lett.*, vol. 14, no. 2, pp. 179–183, Feb. 2016.
[13] L. He, R. Panciera, M. A. Tanase, J. P. Walker, and Q. Qin, "Soil moisture retrieval in agricultural fields using adaptive model-based polarimetric decomposition of SAR data," *IEEE Trans. Geosci. Remote Sens.*, vol. 54, no. 8, pp. 4445–4460, Aug. 2016.
[14] L. Zhu, J. P. Walker, N. Ye, and C. Rudiger, "The effect of radar configuration on effective correlation length," in *Proc. 2016 Int. Conf. Electromagn. Adv. Appl.*, 2016, pp. 820–823.
[15] R. Panciera, M. A. Tanase, K. Lowell, and J. P. Walker, "Evaluation of IEM, Dubois, and Oh radar backscatter models using airborne L-band SAR," *IEEE Trans. Geosci. Remote Sens.*, vol. 52, no. 8, pp. 4966–4979, Aug. 2014.
[16] M. A. Tanase, R. Panciera, K. Lowell, J. Hacker, and J. P. Walker, "Estimation of forest biomass from L-band polarimetric decomposition components," in *Proc. 2013 IEEE Int. Geosci. Remote Sens. Symp.*, 2013, pp. 949–952.
[17] M. A. Tanase, R. Panciera, K. Lowell, C. Aponte, J. M. Hacker, and J. P. Walker, "Forest biomass estimation at high spatial resolution: Radar versus lidar sensors," *IEEE Geosci. Remote Sens. Lett.*, vol. 11, no. 3, pp. 711–715, Mar. 2014.
[18] M. A. Tanase, R. Panciera, K. Lowell, S. Tian, J. M. Hacker, and J. P. Walker, "Airborne multi-temporal L-band polarimetric SAR data for biomass estimation in semi-arid forests," *Remote Sens. Environ.*, vol. 145, pp. 93–104, 2014.
[19] Y. Huang, J. P. Walker, Y. Gao, X. Wu, and A. Monerris, "Estimation of vegetation water content from the radar vegetation index at L-band," *IEEE Trans. Geosci. Remote Sens.*, vol. 54, no. 2, pp. 981–989, Feb. 2016.
[20] M. Tanase, R. Panciera, K. Lowell, and C. Aponte, "Monitoring live fuel moisture in semiarid environments using L-band radar data," *Int. J. Wildland Fire*, vol. 24, no. 4, pp. 560–572, 2015.
[21] S. Elhassan, X. Wu, and J. P. Walker, "Standing water detection using radar," in *Proc. 20th Int. Congr. Model. Simul.*, 2013, pp. 3085–3091.
[22] A. E. Giraldez, "SAOCOM-1 Argentina L-band SAR mission overview," in *Proc. Coastal Marine Appl. SAR Symp.*, 2003.
[23] C. Menges, R. Bartolo, D. Bell, and G. E. Hill, "The effect of savanna fires on SAR backscatter in northern Australia," *Int. J. Remote Sens.*, vol. 25, no. 22, pp. 4857–4871, 2004.
[24] A. Freeman, "SAR calibration: An overview," *IEEE Trans. Geosci. Remote Sens.*, vol. 30, no. 6, pp. 1107–1121, Nov. 1992.
[25] P. C. Dubois, D. Evans, and J. V. Zyl, "Approach to derivation of SIR-C science requirements for calibration," *IEEE Trans. Geosci. Remote Sens.*, vol. 30, no. 6, pp. 1145–1149, Nov. 1992.
[26] A. Freeman, Y. Shen, and C. L. Werner, "Polarimetric SAR calibration experiment using active radar calibrators," *IEEE Trans. Geosci. Remote Sens.*, vol. 28, no. 2, pp. 224–240, Mar. 1990.
[27] A. L. Gray, P. W. Vachon, C. E. Livingstone, and T. I. Lukowski, "Synthetic aperture radar calibration using reference reflectors," *IEEE Trans. Geosci. Remote Sens.*, vol. 28, no. 3, pp. 374–383, May 1990.
[28] K. Sarabandi *et al.*, "Polarimetric calibration of SIR-C using point and distributed targets," *IEEE Trans. Geosci. Remote Sens.*, vol. 33, no. 4, pp. 858–866, Jul. 1995.
[29] E. L. Christensen *et al.*, "EMISAR: An absolutely calibrated polarimetric L-and C-band SAR," *IEEE Trans. Geosci. Remote Sens.*, vol. 36, no. 6, pp. 1852–1865, Nov. 1998.
[30] M. Shimada, O. Isoguchi, T. Tadono, and K. Isono, "PALSAR radiometric and geometric calibration," *IEEE Trans. Geosci. Remote Sens.*, vol. 47, no. 12, pp. 3915–3932, Dec. 2009.
[31] K. Sarabandi *et al.*, "Cross-calibration experiment of JPL AIRSAR and truck-mounted polarimetric scatterometer," *IEEE Trans. Geosci. Remote Sens.*, vol. 32, no. 5, pp. 975–985, Sep. 1994.
[32] M. Shimada, "Model-based polarimetric SAR calibration method using forest and surface-scattering targets," *IEEE Trans. Geosci. Remote Sens.*, vol. 49, no. 5, pp. 1712–1733, May 2011.
[33] T. L. Ainsworth, L. Ferro-Famil, and J.-S. Lee, "Orientation angle preserving a posteriori polarimetric SAR calibration," *IEEE Trans. Geosci. Remote Sens.*, vol. 44, no. 4, pp. 994–1003, Apr. 2006.
[34] M. Gupta, A. Sharma, and B. Kartikeyan, "Evaluation of RISAT-1 SAR radiometric calibration using extended amazon rainforest," *J. Indian Soc. Remote Sens.*, vol. 45, pp. 195–207, 2016.
[35] M. Zink, P. Olivier, and A. Freeman, "Cross-calibration between airborne SAR sensors," *IEEE Trans. Geosci. Remote Sens.*, vol. 31, no. 1, pp. 237–245, Jan. 1993.
[36] S. Jaruwatanadilok, B. W. Stiles, and A. G. Fore, "Cross-calibration between QuikSCAT and Oceansat-2," *IEEE Trans. Geosci. Remote Sens.*, vol. 52, no. 10, pp. 6197–6204, Oct. 2014.
[37] N. Ye, J. P. Walker, and C. Rüdiger, "A cumulative distribution function method for normalizing variable-angle microwave observations," *IEEE Trans. Geosci. Remote Sens.*, vol. 53, no. 7, pp. 3906–3916, Jul. 2015.
[38] G. R. S. AG, "Modular SAR processor–MSP documentation users guide (Version 1.6)," Documentation Users Guide (Version 1.6), Gümligen, Switzerland 2009.
[39] A. G. Fore *et al.*, "UAVSAR polarimetric calibration," *IEEE Trans. Geosci. Remote Sens.*, vol. 53, no. 6, pp. 3481–3491, Jun. 2015.
[40] N. Chamberlain, M. Zawadzki, G. Sadowy, E. Oakes, K. Brown, and R. Hodges, "The UAVSAR phased array aperture," in *Proc. IEEE Aerosp. Conf.*, 2006, pp. 1–12.
[41] F. T. Ulaby *et al.*, *Microwave Radar and Radiometric Remote Sensing*. Ann Arbor, MI, USA: Univ. Michigan Press, 2014.
[42] A. Freeman and S. L. Durden, "A three-component scattering model for polarimetric SAR data," *IEEE Trans. Geosci. Remote Sens.*, vol. 36, no. 3, pp. 963–973, May 1998.
[43] D. Kahny and J. van ZyI, "How does corner reflector construction affect polarimetric sar-calibration?," in *Proc. 10th Annu. Int. Symp. Geosci. Remote Sens. Symp.*, 1990, pp. 1093–1097.
[44] C. Craeye, P. Sobieski, E. Robin, and A. Guissard, "Angular errors in trihedrals used for radar calibrations," *Int. J. Remote Sens.*, vol. 18, no. 12, pp. 2683–2689, 1997.
[45] M. Shimada, M. Watanabe, T. Motooka, and Y. Kankaku, "PALSAR-2 polarimetric performance and the simulation study using the PI-SAR-L2," in *Proc. 2013 IEEE Int. Geosci. Remote Sens. Symp.*, 2013, pp. 2309–2312.

Liujun Zhu received the B.S. degree in geography from Zhejiang Normal University, Jinhua, China, in 2012, and the M.Sc. degree in geography information science from Nanjing University, Nanjing, China, in 2015. He is currently working toward the Ph.D. degree in civil engineering at Monash University, Melbourne, VIC, Australia.

During 2017–2018, he was a visiting Ph.D. student with the University of Michigan-Ann Arbor, Ann Arbor, MI, USA. His current research interests include active microwave remote sensing, soil moisture retrieval, machine learning, and its applications in classification and change detection.

Jeffrey P. Walker received the B.E. degree in civil and the B. Surveying degree with first class honors and the university medal in 1995, and the Ph.D. degree in water resources engineering from The University of Newcastle, Callaghan, NSW, Australia, in 1999.

His Ph.D. dissertation was among the early pioneering research on estimation of root-zone soil moisture from assimilation of remotely sensed surface soil moisture observations. Then, he joined NASA Goddard Space Flight Centre to implement his soil moisture work globally. In 2001, he was a Lecturer with the Department of Civil and Environmental Engineering, University of Melbourne, where he continued his soil moisture work, including development of the only Australian airborne capability for simulating new satellite missions for soil moisture. In 2010, he was a Professor with the Department of Civil Engineering, Monash University, Melbourne, VIC, Australia, where he is continuing this research. He is contributing to soil moisture satellite missions at NASA, Washington, DC, USA, ESA, Paris, France, and JAXA, Tokyo, Japan, as a Science Team member for the Soil Moisture Active Passive mission and Cal/Val Team member for the Soil Moisture and Ocean Salinity and the Global Change Observation Mission—Water, respectively.

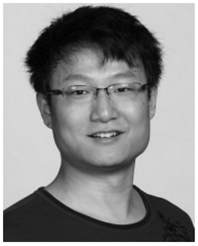

Nan Ye received the B.E. degree in hydraulic and hydropower engineering from Tsinghua University, Beijing, China, in 2006, and the Ph.D. degree in civil engineering from Monash University, Melbourne, VIC, Australia, in 2014.

In 2013, he was with the Department of Geographic Information Science, Nanjing University, Nanjing, China, worked on snow properties retrievals from optical and SAR data. In 2014, he returned to Monash University, where he coordinated a number of airborne field experiments for the in-orbit calibration/validation of the Soil Moisture Active Passive mission in the Murrumbidgee river catchment, southeast of Australia. He is currently a Senior Research Fellow with Monash University working on *P*-band passive microwave remote sensing of soil moisture.

Christoph Rüdiger (M'10–SM'15) received the B.E. degree in civil engineering from the University of Applied Sciences, Wiesbaden (now Rhein-Main), Germany, in 2002, and the Ph.D. degree in environmental engineering from the University of Melbourne, Melbourne, VIC, Australia, in 2008, with a focus on the potential to assimilate streamflow data into land surface models for soil moisture prediction.

His undergraduate thesis covered the topic of groundwater and contaminant flow around submerged building structures. He joined the Centre National de Recherches Météorologiques, Météo-France, Toulouse, France, in 2006, focusing on the performance analysis and data assimilation of surface soil moisture and LAI within the French land surface model ISBA. This was followed by a post-doctoral position financed by the French Space Agency on the validation of different passive and active microwave satellite products over France, with a particular focus on ESA's SMOS mission. He returned to Australia in 2008, on a position to coordinate and lead a number of Cal/Val campaigns for the Australian land validation segment of the SMOS mission in the Australian arid zone and the Murrumbidgee river catchment. Since 2011, he has been a faculty member with the Department of Civil Engineering, Monash University, Melbourne, VIC, Australia. Since then, he has participated in the Australian Cal/Val segments for NASA's SMAP and Aquarius missions, and is a PI on JAXA's GCOM-C mission. His current research interests include the remote sensing of vegetation dynamics and landscape water content at high resolution for drought monitoring and wildfire predictions, and the development of low-cost environmental monitoring networks.

Jörg M. Hacker received the Doctorate degree in atmospheric sciences (Dr. rer. nat.) from the Meteorological Institute of the University of Bonn, Bonn, Germany, in 1980.

In 1982, he was a Postdoctoral Fellow with the Flinders University, Adelaide, SA, Australia. There, from very small beginnings, he built up Australia's National Research Aircraft Facility *ARA—Airborne Research Australia*, which today is Australia's only National Facility engaged in using and operating aircraft for atmospheric and environmental research. He is the ARA's Director and a Chief Scientist, and also holds professorial status within Flinders University. In 2015, he led the establishment of ARA as an independent not-for-profit research institute funded substantially by the Hackett Foundation in Adelaide. He has coauthored more than 100 publications in internationally refereed journals and 170 conference papers. His research interests include a wide area, with special emphasis on the atmospheric boundary layer, very high resolution airborne remote sensing, and the development of innovative instrumentation and measurement strategies using airborne platforms. He pioneered the concept of using cost-efficient small aircraft for environmental research, including the research described in this paper.

Rocco Panciera, photograph and biography not available at the time of publication.

Mihai A. Tanase, photograph and biography not available at the time of publication.

Xiaoling Wu received the B.E. degree in biomedical engineering from Zhejiang University, Hangzhou, China, in 2009, and the Ph.D. degree in civil engineering from Monash University, Melbourne, VIC, Australia, in 2015.

The topic of her undergraduate thesis was development of biosensor using nanomaterial. She was a visiting scholar in the Department of Computer Science, University of Copenhagen, Denmark, from 2009 to 2010. The topic of her Ph.D. research was downscaling of soil moisture using airborne radar and radiometer observations in order to provide an accurate and high resolution (better than 10 km) soil moisture product with potential benefit in the areas of weather forecasting, flood, and drought prediction, agricultural activities, etc. She is the Research Fellow with Monash University and continuing high-resolution soil moisture work. Her research interests include microwave remote sensing of soil moisture, soil moisture downscaling, and proximal soil moisture sensing for real-time agricultural applications.

Douglas A. Gray received the Ph.D. degree from the University of Adelaide, Adelaide, SA, Australia, in 1973.

He spent 20 years with the Australian Defence Science and Technology Organisation applying signal processing to sonar and electronic warfare leading various research and development programs. From 1993 to 2006, he was the Deputy Director of the Cooperative Research Centre for sensor signal and information processing and led a number of programs and projects in radar, sonar, and GPS. In 2010, he founded the University of Adelaide Radar Research Centre and served as the Director until 2015, focusing on the use of radar for environmental monitoring and surveillance. He retired in 2016 and is an emeritus Professor with the University of Adelaide. His current research interests include array processing, radar for monitoring weather and bushfires, and synthetic aperture radar for surveillance and environmental monitoring.

Nick Stacy, photograph and biography not available at the time of publication.

Alvin Goh, photograph and biography not available at the time of publication.

Heath Yardley, photograph and biography not available at the time of publication.

Jim Mead (S'86–M'89–SM'99) received the B.S.E.E. degree from the University of Virginia, Charlottesville, VA, USA, in 1981, and the Ph.D. degree from the University of Massachusetts, Amherst, MA, USA, in 1989.

From 1981 to 1986, he was with Singer Kearfott Division, Wayne, NJ, USA, where he designed microstrip and leaky wave antennas for Doppler navigation systems. In June 1986, he joined the Microwave Remote Sensing Laboratory, University of Massachusetts, where his graduate work involved the development of millimeter-wave polarimetric radars at 95 and 225 GHz, and the use of millimeter-wave radars for cloud research. From 1990 to 1996, he was with the University of Massachusetts, where he was a Senior Research Fellow and later a Research Associate Professor. His research interests include radar polarimetry and the development of digital beamforming radar systems for atmospheric and oceanographic applications.

Since 1996, Dr. Mead has been the President of ProSensing, Inc., which specializes in custom radar and radiometer systems for environmental remote sensing applications.